Check for updates

3D Microscale Flow Simulation of Shear-Thinning Fluids in a Rough Fracture

Min Zhang[1] · Maša Prodanović[1] · Maryam Mirabolghasemi[2] · Jianlin Zhao[3]

Abstract

The shear-thinning fluid flow in rough fractures is of wide interest in subsurface engineering. Inertial effects due to flow regime, fracture aperture variations as well as fluid rheology affect the macroscopic flow parameters in an interrelated way. We present a 3D microscale flow simulation for both Newtonian and Cross power-law shear-thinning fluids through a rough fracture over a range of flow regimes, thus evaluating the critical Reynolds number above which the linear Darcy's law is no longer applicable. The flow domain is extracted from a computed microtomography image of a fractured Berea sandstone. The fracture aperture is much more variable than any of the previous numerical or experimental work involving shear-thinning fluids, and simulations are 3D for the first time. We quantify the simulated velocity fields and propose a new correlation for shift factor (parameter relating in situ porous medium viscosity with bulk viscosity). The correlation incorporates tortuosity (parameter calculated either based only on fracture image or on detailed velocity field, if available) as well as a fluid-dependent parameter obtained from the analytical/semi-analytical solutions of the same shear-thinning fluids flow in a smooth slit. Our results show that the shift factor is dependent on both the fracture aperture distribution (not only the hydraulic/equivalent aperture) and fluid rheology properties. However, both the inertial coefficient and critical Reynolds number are functions of the fracture geometry only, which is consistent with a recent experimental study.

Keywords Shear-thinning fluid · Computational fluid dynamics · Realistic rough fracture · Forchheimer's law · Shift factor

1 Introduction

The scientific problem of shear-thinning fluid flow in the rough fracture is encountered in numerous industrial applications such as the hydraulic fracturing fluids (slick water, polymer gels or foams; often carrying proppants) flow in rough hydraulic and natural fractures (Osiptsov 2017; Liu and Sharma 2005; Liu 2006; Huang et al. 2017b; Raimbay et al. 2016;

✉ Min Zhang
  minzhang@utexas.edu

Extended author information available on the last page of the article

Huang et al. 2017a), polymer gel extrusion through rough fractures to reduce excessive water production in naturally fractured reservoirs (Wang et al. 2017; Seright 2001, 1999, 2003), CO_2 sequestration and potential leakage through rough fractures (Huo and Gong 2010; Shukla et al. 2010; Hawkes et al. 2004), drilling fluids infiltration into fractures intersecting the wellbore (Feng and Gray 2017a, b; Feng et al. 2016), and foam applications (mainly as a mobility-control fluid) in environmental remediation and other subsurface engineering (Kovscek et al. 1995). However, due to the complexities of both the porous medium geometry and non-Newtonian fluid behavior, the flow characteristics, including both the prediction of macroscopic pressure drop and the underlying physical nature, of these complex shear-thinning fluids in the rough fractures remain poorly understood.

For Newtonian fluids (of constant viscosity μ), the shear stress τ is directly proportional to the shear rate $\dot{\gamma}$, $\tau = \mu\dot{\gamma}$. All those fluids for which the above proportionality is violated are said to be non-Newtonian (Sochi 2010). Some, but not all, flow characteristics of non-Newtonian fluids include strain- and time-dependent viscosity, yield-stress and stress relaxation (Sochi 2010). In engineering practice, we are primarily interested in the viscosity behavior of non-Newtonian fluids, and thus the generalized Newtonian models with dynamically upscaled viscosity have been widely used by engineers. Therefore, a large number of rheological models have been proposed in the literature, such as power-law, Ellis, Carreau, Cross, Herschel–Bulkley. Table 1 in Sochi (2010) gives a few prominent examples of non-Newtonian rheological models.

Numerous studies on shear-thinning fluids (whose viscosity decreases as the shear rate increases) flow in porous matrix have been conducted since 1980s, including the experimental (Chauveteau 1982; Comba et al. 2011; Perrin et al. 2006; Rodríguez de Castro and Radilla 2017b), theoretical (Hayes et al. 1996; Liu and Masliyah 1999) and numerical studies. Specifically, for the numerical studies, most work was based on pore network models (Pearson and Tardy 2002; Sorbie et al. 1989; Lopez et al. 2003; Perrin et al. 2006; Balhoff et al. 2012) due to their high computational efficiency. There is also some work on direct simulation of non-Newtonian fluids flow in 2D porous medium (Tosco et al. 2013). However, the flow of shear-thinning fluids through rough fractures has only been addressed recently.

Rodríguez de Castro and Radilla (2016) conducted inertial/non-Darcian flow experiments of shear-thinning fluids described as Carreau fluids through two rough-walled rock fractures (a granite fracture and a Vosges sandstone fracture). Their findings show that the non-Darcian flow law could be extended to the shear-thinning fluids flow through rough-walled rock fractures and the inertial coefficients could be obtained by the non-Darcian Newtonian flow experiments, which means that the inertial coefficients are not dependent on the fluid rheology properties. Then, they obtained the shift factor α for each porous medium-fluid pair. Specifically, α is an empirical shift factor relating in situ porous medium viscosity (μ_{pm}) to bulk viscosity, and known to be a function of both the bulk rheology of the fluid and the porous media (please see Sect. 2.1 for more details about the definitions and physical meanings of the above parameters). Rodríguez de Castro and Radilla (2017a) further conducted the linear/Darcian shear-thinning fluid flow experiments through the same rough-walled rock fractures. They derived the flow rate-dependent shift factor α expressions for the commonly used Carreau and yield-stress fluids in parallel plate model based on the Weissenberg–Rabinowitsch–Mooney theory (Macosko 1994; Pipe et al. 2008). Based on the two investigated rough-walled rock fractures in their work, they concluded that the fracture aperture distributions have no significant effects on the shift factor α, and only the "hydraulic/equivalent aperture w_{eq}" is included in their α expressions.

According to a lot of the above-mentioned research work on non-Newtonian fluids flow in porous media, the shift factor α should be a function of both fluid rheology properties and porous medium geometry. For rough fractures, a hydraulic (equivalent) aperture might not be enough to take into account the complicated microscopic fracture aperture distribution and its variations. To validate the above hypothesis, the microscopic fracture aperture distributions should be quantified and then correlated with the shear-thinning fluid flow behavior. However, this is difficult for the traditional experiments. Fortunately, the direct microscale flow simulations provide an alternative, and we pursue it in this work.

From the viewpoint of direct numerical simulation, the flow of shear-thinning fluids in rough fractures involves two critical issues: one is the complex geometry of realistic rough fractures (Noiriel et al. 2013, 2007; Crandall et al. 2010; Briggs et al. 2017; Zou et al. 2015) (which could result in some discretization issues) and the other is the fluid rheology of shear-thinning fluids (Sochi 2010). Fluid flow in a rough-walled rock fracture represents a multi-scale problem: the fracture aperture is orders of magnitude smaller than the other two in-plane dimensions (Lavrov 2013a; Cardenas et al. 2009). Therefore, the fully 3D resolution of the flow field can be very computationally expensive and even computationally prohibitive.

A popular way to reduce the computational cost of 3D simulation of Navier–Stokes equations in rough fractures is the lubrication theory approximation (Zimmerman et al. 1991; Zimmerman and Bodvarsson 1996; Ge 1997; Xiao et al. 2013; Brush and Thomson 2003; Konzuk and Kueper 2004; Wang et al. 2015; Renshaw 1995). Lubrication theory approximation converts the 3D problem into a quasi 3D problem through averaging the velocity field across the fracture aperture, which will eliminate the dimension along the fracture aperture. For the Newtonian fluids flow in rough fractures, a lot of research work has been done and the conditions under which the lubrication theory approximation is valid have been well established (Zimmerman et al. 1991; Zimmerman and Bodvarsson 1996). Because of its much less computational costs, the lubrication theory approximation has been widely used to simulate non-Newtonian fluids flow in rough fractures (Di Federico 1998, 2001; Lavrov 2013b, c, 2014, 2015; Felisa et al. 2017; Talon et al. 2014). Although some preliminary experimental work has been conducted to validate the applicability of lubrication theory to power-law fluids (Ciriello et al. 2016) and Herschel–Bulkley fluids (Di Federico et al. 2017), due to the extreme complexity of this problem, it is still unclear whether the lubrication theory approximation or a similar approach applies for non-Newtonian fluids and under what conditions (Lavrov 2013a).

In addition, some researchers studied the direct simulation of non-Newtonian fluids flow in rough-walled fractures with computational fluid dynamics (CFD) (Roustaei et al. 2016) or Lattice Boltzmann method (LBM) (Yan and Koplik 2008; Dharmawan et al. 2016). However, these are 2D simulations. To our best knowledge, solving the Navier–Stokes equations combined with the shear-thinning fluid rheology model with fully 3D flow field in the realistic rough fracture has not been done to date.

In this paper, for the first time, a 3D microscale flow simulation of Cross power-law shear-thinning fluids in a realistic rough fracture is conducted. The main contribution of this work is to propose a new shift factor α correlation for the case of shear-thinning fluids flow in a rough fracture. In the remaining sections of the paper, a detailed description of the governing equations for shear-thinning fluids flow in the rough fracture is given in Sect. 2. In addition, the microscale flow simulation and its validation will also be introduced in Sect. 2. In Sect. 3, both the macroscopic results and microscopic flow patterns are analyzed. Our newly proposed shift factor α correlation is discussed in Sect. 4. Finally, Sect. 5 summarizes our work and gives recommendations for future work.

2 Methodology

2.1 Non-Darcian Flow of Shear-Thinning Fluids in a Rough Fracture

For the laminar flow of Newtonian fluids in porous media, Darcy's law is used to describe the linear relationship between pressure drop and flow rate:

$$-\frac{\Delta P}{L} = \frac{\mu}{K}\frac{Q}{A} \tag{1}$$

where P is the fluid pressure [$ML^{-1}T^{-2}$], L is the porous medium sample length [L], μ is the (constant) viscosity of Newtonian fluid [$ML^{-1}T^{-1}$], K is the intrinsic permeability [L^2], Q is the flow rate [L^3T^{-1}], and A is the cross-sectional area [L^2] of the porous medium sample.

The linear Darcy's law becomes invalid with the increase in Reynolds number, when the inertial forces can no longer be ignored compared with the viscous forces. Forchheimer's equation (Forchheimer 1901) has been widely used to describe the nonlinear relationship between pressure drop and flow rate in the strong inertial regime (Rodríguez de Castro and Radilla 2016):

$$-\frac{\Delta P}{L} = \frac{\mu}{K}\frac{Q}{A} + \beta\rho\left(\frac{Q}{A}\right)^2 \tag{2}$$

where β is the inertial coefficient [L^{-1}] and ρ is the (constant) fluid density [ML^{-3}].

For non-Newtonian fluids flow in porous media, the assumption of constant viscosity in above equations is invalid since the "bulk" viscosity of non-Newtonian fluids is a function of shear rate, $\mu(\dot{\gamma})$. Therefore, in order to describe the macroscopic flow behavior of non-Newtonian fluids flow in porous media accurately and efficiently, several important parameters are defined as follows.

The first parameter is "porous medium (in-situ) viscosity, μ_{pm}" (Bird et al. 1987) which is used for non-Newtonian fluids in the above macroscopic relationships between pressure drop and flow rate to replace the constant Newtonian viscosity μ:

For the laminar flow:

$$-\frac{\Delta P}{L} = \frac{\mu_{pm}}{K}\frac{Q}{A} \tag{3}$$

For the strong inertial regime:

$$-\frac{\Delta P}{L} = \frac{\mu_{pm}}{K}\frac{Q}{A} + \beta\rho\left(\frac{Q}{A}\right)^2 \tag{4}$$

The above modified equations are based on the hypothesis that the macroscopic flow laws for Newtonian fluids can be extended to non-Newtonian fluids, which has been verified in the literature with microscale flow simulation in 2D porous media (Tosco et al. 2013) and experimental results (Rodríguez de Castro and Radilla 2016, 2017b, a). Specifically, the shear-thinning fluid models investigated in Tosco et al. (2013) include Cross, Ellis and Carreau, and Rodríguez de Castro and Radilla (2017b) conducted the experiments of Carreau fluids through packed beads. The experiments of Rodríguez de Castro and Radilla (2016) and Rodríguez de Castro and Radilla (2017a) have been introduced in detail in Sect. 1. One objective of this work is to validate this assumption using 3D microscale flow simulations in a realistic rough fracture geometry.

Instead of the simple power-law fluid constitutive rheology model which cannot characterize the real fluids at both low and high shear rates (Felisa et al. 2017), we mainly focus on the four-parameter Cross power-law shear-thinning model with asymptotic values of viscosity at both upper and lower limits:

$$\mu = \mu_\infty + \frac{\mu_0 - \mu_\infty}{[1 + m^n(\dot{\gamma})^n]} \tag{5}$$

where μ_0 and μ_∞ are the upper and lower Newtonian plateaus $[ML^{-1}T^{-1}]$, respectively, m is the time constant $[T]$, n is the power-law index, $\dot{\gamma}$ is shear rate $[T^{-1}]$.

μ_{pm} can be calculated based on the "porous medium shear rate, $\dot{\gamma}_{pm}$":

$$\mu_{pm} = \mu_\infty + \frac{\mu_0 - \mu_\infty}{[1 + m^n(\dot{\gamma}_{pm})^n]} \tag{6}$$

For practical field applications of non-Newtonian fluids flow in porous media, extensive work has been done to relate the "bulk" viscometric behavior of non-Newtonian fluids (Eq. (5)) to its "observed/apparent" behavior in the porous medium (Eq. (6)) (Christopher and Middleman 1965; James and McLaren 1975; Chauveteau 1982; Sorbie et al. 1989). In order to calculate μ_{pm} based on the "bulk" viscosity formula (Eq. (5)), the second parameter, the effective shear rate with the porous medium $\dot{\gamma}_{pm}$, should be defined. According to the dimensional analysis, there should be a characteristic length $[L]$ to relate shear rate $[T^{-1}]$ and Darcy velocity $[LT^{-1}]$, and one approximation of this characteristic length is $\sqrt{K\phi}$ (Lopez et al. 2003), where ϕ is the porous medium porosity. Therefore, the initial/intuitive definition of porous medium shear rate is $\dot{\gamma}_{pm} = |v|/\sqrt{K\phi}$, where $|v|$ is the Darcy velocity $[LT^{-1}]$. However, when this definition is substituted into Eq. (6), there is a shift between the true porous medium viscosity and the calculated value versus measured/average shear rate curves. Therefore, the third parameter "shift factor α" (Sorbie et al. 1989) was introduced into this definition:

$$\dot{\gamma}_{pm} = \alpha \frac{|v|}{\sqrt{K\phi}} = \alpha \frac{\sqrt{12}Q}{w_{eq}^2 W} \tag{7}$$

where w_{eq} is the hydraulic/equivalent aperture of a rough fracture obtained from Newtonian Darcian flow simulations $[L]$, W is the fracture width $[L]$, K is the permeability of a rough fracture, $K = \frac{w_{eq}^2}{12}$, and ϕ is assumed to be 1 for fracture geometry.

Based on the definitions of μ_{pm} and $\dot{\gamma}_{pm}$ and also the basic assumption of steady-state laminar flow (the only assumption of steady-state laminar flow is needed for the simple tube and narrow slit model; while for porous medium, more assumptions would be needed), the expressions of shift factor α could be derived for very simple fluid rheology model and very simple geometries. Table 1 gives the expressions of shift factor α for several very simple cases. Please refer to Appendix A for the derivation of the shift factor α in the cases of simple power-law fluid flow in a tube and a narrow slit. From Table 1, we can clearly see that the shift factor α is a function of both the fluid rheology (since the α expressions involve the power-law index n) and the geometry (since for different geometries the α expressions are different). However, there have not been any satisfying correlations of α for the non-Newtonian fluids flow in complex geometries in the literature, and the range reported is approximately $1 - 15$ (Lopez et al. 2003). In this work, based on a large number of 3D microscale flow simulations, a correlation for shift factor α is obtained for shear-thinning fluids flow in a rough fracture.

Table 1 Shift factor α for several very simple cases

Model	Formulation of α*	Reference
Simple power-law fluid flow in a tube	$\sqrt{2}\left(\frac{3n+1}{4n}\right)^{\frac{n}{n-1}}$	This work
Simple power-law fluid flow in a slit	$\sqrt{3}\left(\frac{2n+1}{3n}\right)^{\frac{n}{n-1}}$	This work
Simple power-law fluid flow in a sphere pack	$\frac{12}{\sqrt{150}}\left(\frac{3n+1}{4n}\right)^{\frac{n}{n-1}}$	Hirasaki and Pope (1974)
	$\frac{12}{\sqrt{150}}\left(\frac{3n+1}{4n}\right)$	Christopher and Middleman (1965)
	$\frac{3n+1}{\sqrt{8n}}$	Sorbie et al. (1989)

*n is the power-law index of the simple power-law fluid rheology model ($\mu = K'(\dot{\gamma})^{n-1}$, where K' is the consistency index of power-law fluid [$ML^{-1}T^{n-2}$])

For convenience, we define "average shear rate" for non-Newtonian fluids flow in a rough fracture as follows (Rodríguez de Castro and Radilla 2016, 2017a) (same as Eq. (7), ϕ is assumed to be 1 for fracture geometry):

$$\dot{\gamma} = \frac{|v|}{\sqrt{K\phi}} = \frac{\sqrt{12}Q}{w_{\text{eq}}^2 W} \tag{8}$$

Here, "average shear rate" is an effective property for porous medium (the rough fracture in our case) that will be used to report a number of results later on (specifically, Figs. 5, 7, 9, 13).

The fourth parameter called "equivalent viscosity, μ_{eq}" would be used in the following analysis. The equivalent viscosity is defined as the quantity that must replace the viscosity in Darcy's law to result in the same pressure drop actually obtained from the microscale flow simulations (Rodríguez de Castro and Radilla 2016; Tosco et al. 2013). Therefore, both the shear-thinning and inertial effects are encompassed in μ_{eq}. In the case of a rough fracture, μ_{eq} is expressed as:

$$\mu_{\text{eq}} = -\frac{\Delta P/L}{Q}KA = \frac{w_{\text{eq}}^3 W \Delta P}{12LQ} \tag{9}$$

where $\Delta P/L$ and Q are the pressure gradient and flow rate from the microscale flow simulations, respectively.

Comparison of Eqs. (4) and (9) results in the following definition for the equivalent viscosity of non-Darcian non-Newtonian fluids flow:

$$\mu_{\text{eq}} = \mu_{\text{pm}}(\dot{\gamma}_{\text{pm}}) + \beta\rho K\frac{Q}{A} \tag{10}$$

The above μ_{eq} vs. flow rate expression includes two terms. The first one is the linear term describing the shear-thinning effect and dominates at low flow rate (low Re). The second term is the inertial term representing the "pseudo"-increase in equivalent viscosity due to the inertial forces and dominates at high flow rate (high Re).

The last parameter that should be introduced for the non-Newtonian fluids flow in a rough fracture is the Reynolds number (Zhou et al. 2015):

$$Re = \frac{\rho w_{\text{eq}}|v|}{\mu_{\text{pm}}} = \frac{\rho Q}{\mu_{\text{pm}} W} \tag{11}$$
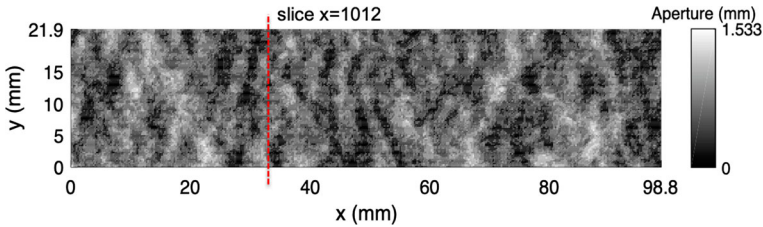
Fig. 1 Berea sandstone fracture aperture field distribution. Asperities (contact points) are where the aperture field is black, and wide parts are where the aperture data are white/light gray. The spacial resolutions are 3040 and 800 in *x*- and *y*-direction, respectively, which is the final resolution used in the following microscale numerical simulations. The red dashed line indicates the selected slice (or cross-section) at *x*=1012, which is the 1012th layer of cells/voxels along the *x*-direction and its physical position is *x*=32.89 mm

Here, μ_{pm} is used instead of μ_{eq} since μ_{pm} only accounts for the viscous forces (or called rheology effects), which is consistent with the definition of Reynolds number as the ratio of inertial to viscous forces (Rodríguez de Castro and Radilla 2016). In addition, a critical value of Reynolds number, Re_c, that delineates the linear and inertial regimes is often used in practical applications. In this work, we adopt the definition of Re_c from Rodríguez de Castro and Radilla (2016), which is a *Re* value for which $\Delta P_{\text{inertial}} = \beta\rho\left(\frac{Q}{A}\right)^2 L$ is approximately 5% of $\Delta P_{total} = \frac{\mu_{\text{pm}}}{K}\frac{Q}{A}L + \beta\rho\left(\frac{Q}{A}\right)^2 L$. Based on the definitions for both Reynolds number (Eq. (11)) and critical Reynolds number, the following formula for critical Reynolds number Re_c could be obtained:

$$Re_c = \frac{12}{19\beta w_{\text{eq}}} \tag{12}$$

2.2 Microscale Flow Simulations

The flow domain was extracted from a computed microtomography (micro-CT) image of a fractured Berea sandstone and the fracture aperture field is shown in Fig. 1 enhanced by the orthogonal view as shown in Fig. 2. The image dimensions are $389 \times 116 \times 25$ voxels, and it has been resampled from the original image that is now publicly available on Digital Rocks Portal (Karpyn et al. 2016). Given that the voxel sizes are 0.26 mm in the longer direction (*x*-direction) and 0.219 mm in the other two directions (*y*- and *z*-direction), the overall size of the fracture is $101 \times 25 \times 5.5$ mm^3. A voxel-based Cartesian grid was used for the flow domain discretization and the detailed routine for converting a digital image to a voxel-based Gmsh mesh file can be found in Mirabolghasemi (2017). During this conversion, the initial image was cut and modified and the finial fracture dimension used in this work is $98.8 \times 21.9 \times 5.5$ mm^3. In a voxel-based grid, each CFD grid cell is a hexahedron with dimensions $0.260 \times 0.219 \times 0.219$ mm^3, the same as the voxel size of the initial image. The initial discretization shown in Fig. 3 was further refined through dividing one hexahedron into 512 (8 in each direction) identical smaller ones and the final number of grid blocks was 47,338,496. This should be ample resolution based on both our sensitivity analysis and that of Crandall et al. (2010) done for Newtonian fluids.

Microscale flow simulations for both Newtonian and shear-thinning fluids in the described rough fracture were conducted by solving continuity equation (Eq. (13)) and steady-state Navier–Stokes equation (Eq. (14)) with the simpleFoam solver in OpenFOAM (https://openfoam.org/) in 3D.
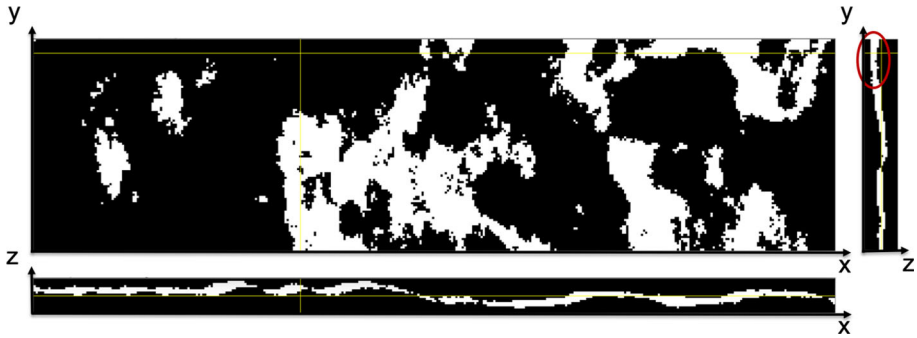
Fig. 2 Orthogonal view of Berea sandstone fracture from Fiji (https://fiji.sc/) (white represents the fracture/pore space and black the solid space), which is essentially three cross-sections along x-, y- and z-direction. The dimension/resolution of this volumetric dataset is $3040 \times 800 \times 128$. The large image in the middle shows the XY view of the 65th layer along z-direction. The image on the right is the YZ view showing segmented geometry of the selected slice $x=1012$ and the upper part indicated with a red ellipse is where the analysis in Sect. 3 will focus on. The image at the bottom is the XZ view of the 748th layer along y-direction. Yellow lines across the views identify locations of the cross-section
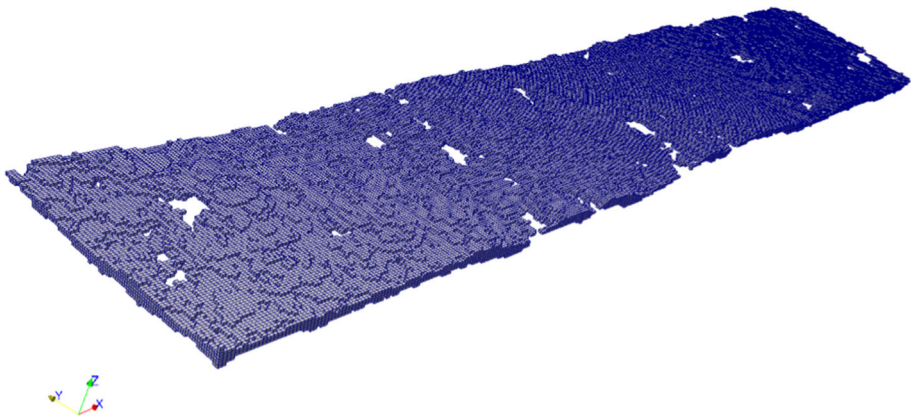
Fig. 3 The initial space discretization (92,458 grid blocks) converted from the digital image (Mirabolghasemi 2017)

$$\nabla \cdot \overrightarrow{\mathbf{U}} = 0 \tag{13}$$

$$\rho \nabla \cdot \left(\overrightarrow{\mathbf{U}}\, \overrightarrow{\mathbf{U}} \right) = -\nabla P + \nabla \cdot \left(\mu \nabla \overrightarrow{\mathbf{U}} \right) \tag{14}$$

where $\overrightarrow{\mathbf{U}}$ is the velocity vector [LT^{-1}].

In total, we conducted two sets of simulations of Newtonian fluids and four sets of shear-thinning fluids. The viscosities of Newtonian fluid #1 and #2 are 3.52 Pa · s and 0.001 Pa · s, respectively. Table 2 gives the values of parameters in Cross power-law fluid rheology model for the four sets of shear-thinning fluids, and the corresponding viscosity curves are shown in Fig. 4.

For all the simulated fluids, a density of 1000 kg/m³ was used. The following boundary conditions were applied in this work which are very popular in similar studies: (1) fixed-pressure boundary conditions in x-direction (the inlet and outlet of the fracture geometry);

Table 2 Values of parameters in Cross power-law fluid rheology model for shear-thinning fluids

Shear-thinning fluids cases	$\mu_0(\text{Pa} \cdot \text{s})$	$\mu_\infty(\text{Pa} \cdot \text{s})$	$m(1/\text{s})$	n
#1	3.52	0.001	10.1	0.62
#2	3.52	0.001	10.1	0.4
#3	3.52	0.1	10.1	0.62
#4	3.52	0.001	1	0.62

Fig. 4 Model curves for the shear viscosity μ as a function of shear rate $\dot{\gamma}$ for four shear-thinning fluids used in the microscale flow simulations
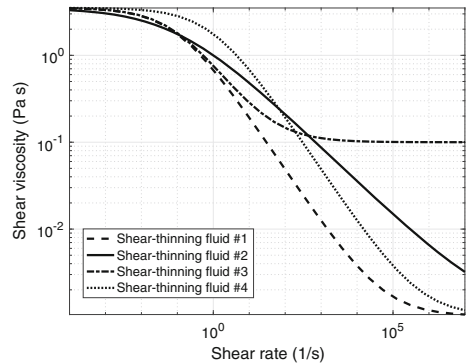
(2) symmetry boundary conditions in y-direction (the lateral sides of the fracture geometry); (3) no-slip boundary conditions in z-direction (the fracture walls).

OpenFOAM v4.1 was used in this work, which was compiled at Lonestar 5 (LS5) machine at Texas Advanced Computing Center (TACC) (https://www.tacc.utexas.edu/). At the time of this work, each computing node of LS5 has two Intel E5-2690 v3 12-core (Haswell) processors (24 cores/node) and 64 GB of DDR4 memory (https://portal.tacc.utexas.edu/user-guides/lonestar5). To give the reader an idea about the complexity of the simulations done in this work, we note that each data point for the rough fracture geometry required 16 processors (1 node) for about 1 hour to 140 hours, which mainly depends on the applied pressure gradient. When the pressure gradient is small, the simulation is fast and when the pressure gradient is very large, then the simulation time is long. Overall, we have run on the order of 200 simulations for this manuscript and used up to around 15,000 SUs (LS5 SUs (Node hours) = number of nodes × wallclock time).

2.3 Model Validation: Flow of Shear-Thinning Fluids in a Narrow Slit

To validate the simulation results of shear-thinning fluids flow in a rough fracture, we compare the semi-analytical solutions and our simulation results for Cross power-law fluids flow in a narrow slit. The detailed derivation of the semi-analytical flow rate solution at a specific pressure gradient can be found in Sochi (2015), and this derivation is based on the application of Weissenberg–Rabinowitsch–Mooney–Schofield method. Here, only the procedure to calculate the semi-analytical flow rate solution is given. Firstly, the rate of shear strain at the slit wall, $\dot{\gamma}_w$, is evaluated numerically based on Eq. (15):

$$\left(\mu_\infty + \frac{\mu_0 - \mu_\infty}{1 + m^n(\dot{\gamma}_w)^n}\right)\dot{\gamma}_w = \frac{B\Delta P}{L} \tag{15}$$

Fig. 5 Comparison of equivalent
viscosity of our simulation results
with the analytical solution
(Sochi 2015)
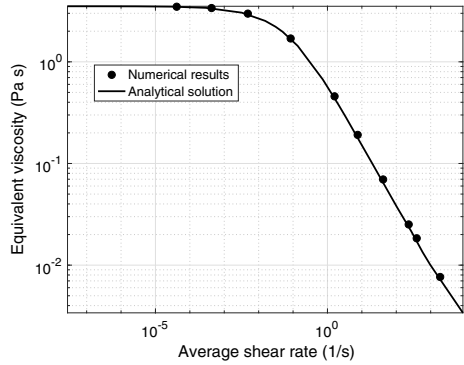
where B is the half slit aperture [L]. Then, the flow rate is obtained from:

$$Q = \frac{2WB^2 I}{\tau_w{}^2} \tag{16}$$

where I is an integral equation,

$$I = \int_0^{\dot{\gamma}_w} \dot{\gamma}^2 \left(\mu_\infty + \frac{\mu_0 - \mu_\infty}{1 + m^n \dot{\gamma}^n} \right) \left(\mu_\infty + \frac{\mu_0 - \mu_\infty}{1 + m^n \dot{\gamma}^n} - \frac{n(\mu_0 - \mu_\infty)m^n \dot{\gamma}^n}{(1 + m^n \dot{\gamma}^n)^2} \right) d\dot{\gamma} \tag{17}$$

and $\tau_w (= \frac{B \Delta P}{L})$ is the wall shear stress. Once the flow rate at a specific pressure gradient is obtained, according to Eqs. (8) and (9), the average shear rate and equivalent viscosity can be calculated, respectively. The comparison of analytical solution and simulation results is shown in Fig. 5, and the largest Reynolds number in our simulations is approximately 1000. It is worth noting that our numerical results consider the inertial terms in Navier–Stokes equations, while the analytical solution does not. The reason why our numerical results match very well with the analytical solution is as follows.

For the analytical solution of Cross power-law fluid flow in a narrow slit and the x-direction is the fluid flow direction, the assumptions are $v_y = v_z = 0$ and $\frac{\partial v_x}{\partial x} = 0$. Therefore, the inertial terms are equal to zero. It means that the analytical solution does not consider the inertial forces/terms. For our numerical results implemented with OpenFOAM, the inertial terms are considered. In a narrow slit, when $Re < 1000$, the flow is laminar and the streamlines are almost straight and then the inertial terms are approximately zero since $v_y \approx 0$, $v_z \approx 0$ and $\frac{\partial v_x}{\partial x} = 0$. Therefore, our numerical results considering inertial forces could match very well with the analytical solution. However, for the laminar flow in a rough fracture, the streamline will deform/bend because of the rough surfaces and then the inertial terms will not be zero (even though it is laminar flow). In addition, with the increase in pressure gradient, the velocity will increase and then the inertial forces will also increase. Therefore, our numerical model could be used to investigate the non-Darcian flow behavior of both Newtonian and shear-thinning fluids in the rough fracture.

3 Results

For the practical field applications, we first study the macroscopic flow behavior of both Newtonian and shear-thinning fluids flow in a rough fracture, including the pressure drop-flow rate relationships and the equivalent viscosity versus average shear rate curves. Then,

taking advantage of the direct pore-scale flow simulations, we quantify tortuosity based on the microscopic flow patterns and provide a new correlation that models the observed macroscopic flow behavior.

3.1 Macroscopic Results

The non-Darcian Forchheimer's law can be extended to the shear-thinning fluids flow in porous media, including 2D porous media (Tosco et al. 2013), packed beads (Rodríguez de Castro and Radilla 2017b) and rough fractures (Rodríguez de Castro and Radilla 2016, 2017a), and the inertial coefficients are only the function of porous medium geometry. Since we simulate a 3D microscale flow of shear-thinning fluids in a realistic rough fracture for the first time, we fit the inertial coefficients of both Newtonian fluids and shear-thinning fluids flow in a rough fracture separately and compare in order to validate the above conclusion from the literature.

3.1.1 Non-Darcian Flow of Newtonian Fluids: Obtaining Hydraulic/Equivalent Aperture w_{eq} and Inertial Coefficient β

The simulation results of pressure gradient versus flow rate for two sets of Newtonian fluids flow in the rough fracture are shown in Fig. 6. To obtain a better fit for the hydraulic aperture and inertial coefficients, a two-step procedure is adopted (Rodríguez de Castro and Radilla 2016).

Step 1: Use the slope of the linear part of pressure gradient versus flow rate curve to obtain the hydraulic aperture. For this fitting, only the $(Q, \Delta P/L)$ data within the strict linear relationship are used and the R-square values are larger than 0.9999. According to Eq. (1), we obtain:

$$k_{\text{slope}} = \frac{\mu}{KA} = \frac{\mu}{\frac{w_{eq}^2}{12} w_{eq} W} = \frac{12\mu}{w_{eq}^3 W} \tag{18}$$

Then, the hydraulic aperture is expressed as:

$$w_{eq} = \left(\frac{12\mu}{W k_{\text{slope}}} \right)^{1/3} \tag{19}$$

Step 2: Once the permeability $K = \frac{w_{eq}^2}{12}$ is obtained, all the $(Q, \Delta P/L)$ data (including both the linear part and nonlinear part) are fitted to Eq. (2) using least square method to obtain the inertial coefficient β. After both w_{eq} and β are obtained, the critical Reynolds number Re_c can be calculated with Eq. (12). All the fitting parameters are given in Table 3.

3.1.2 Non-Darcian Flow of Shear-Thinning Fluids: Obtaining Shift Factor α and Inertial Coefficient β

For shear-thinning fluids, the above two-step procedure is successively used to fit the shift factor α and inertial coefficient β.

Step 1: Fit the porous medium viscosity $\mu_{\text{pm}}(\dot{\gamma}_{\text{pm}})$ versus average shear rate $\dot{\gamma}$ to the equivalent viscosity μ_{eq} versus average shear rate $\dot{\gamma}$ curves to obtain the shift factor α with the least square method. Based on Eq. (10), for linear flow, μ_{eq} will be equal to $\mu_{\text{pm}}(\dot{\gamma}_{\text{pm}})$, where
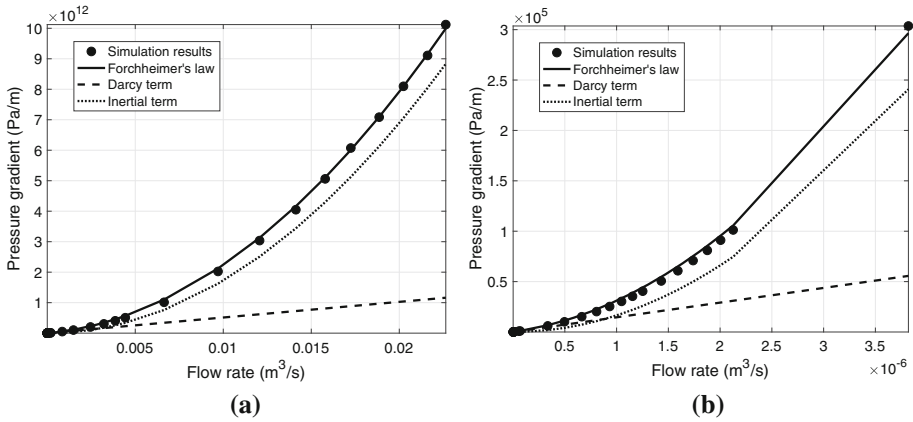
Fig. 6 Pressure gradient versus flow rate for Newtonian fluids flow in the rough fracture. **a** Newtonian fluid #1 ($\mu = 3.52$ Pa · s), **b** Newtonian fluid #2 ($\mu = 0.001$ Pa · s). Symbols represent microscale simulation results. Solid line is the fitted Forchheimer's equation. Dot-dashed and dashed lines are the inertial term and Darcy term in Forchheimer's equation, respectively. The growing discrepancy between "Simulation results" (matching very well with the fitted "Forchheimer's law") and "Darcy term" shows that the inertial pressure losses are becoming dominating with the increase in flow rate

Table 3 Parameters calculated from microscale flow simulation results for both Newtonian and shear-thinning fluids in both rough fracture and narrow slit model

Parameter	Newtonian fluid #1	#2	Shear-thinning fluid #1	#2	#3	#4
w_{eq}(m)	3.35×10^{-4}	3.35×10^{-4}	–	–	–	–
β(m^{-1})	9.27×10^2	8.89×10^2	9.10×10^2	8.97×10^2	9.12×10^2	8.81×10^2
α(−)	–	–	1.68	1.70	1.65	1.70
$\alpha_{slit}(f(n))$(−)	–	–	1.46	1.32	1.37	1.44
$\frac{\alpha}{\alpha_{slit}}$(−)	–	–	1.15	1.295	1.20	1.18
Re_c(−)	2.03	2.12	2.07	2.10	2.07	2.14

μ_{eq} is calculated from the microscale simulation results (Q, $\Delta P/L$) based on Eq. (9) and $\mu_{pm}(\dot{\gamma}_{pm})$ is evaluated by Eq. (6). Figure 7 shows that a very good overlay is obtained for all four sets of shear-thinning fluids simulations and the fitted shift factor α are given in Table 3.

Step 2: Once the shift factor α is obtained, all the ($\dot{\gamma}$, μ_{eq}) data are fitted to Eq. (10) using the least square method and the fitted inertial coefficient β are given in Table 3. After β is obtained, the critical Reynolds number Re_c can be calculated using Eq. (12) where w_{eq} is the fitted parameter from Newtonian fluid flow simulations (Sect. 3.1.1). In addition, with the fitted shift factor α and inertial coefficient β, the pressure gradient versus flow rate curves for four sets of shear-thinning fluids flow in the rough fracture are given in Fig. 8.

### 3.1.3 Comparison of Flow Behavior Between Newtonian and Shear-Thinning Fluids

The comparison of equivalent viscosity curves between Newtonian fluids and shear-thinning fluids is shown in Fig. 9. Based on Eqs. (10) and (8), the inertial term in Eq. (10) has the following expression:
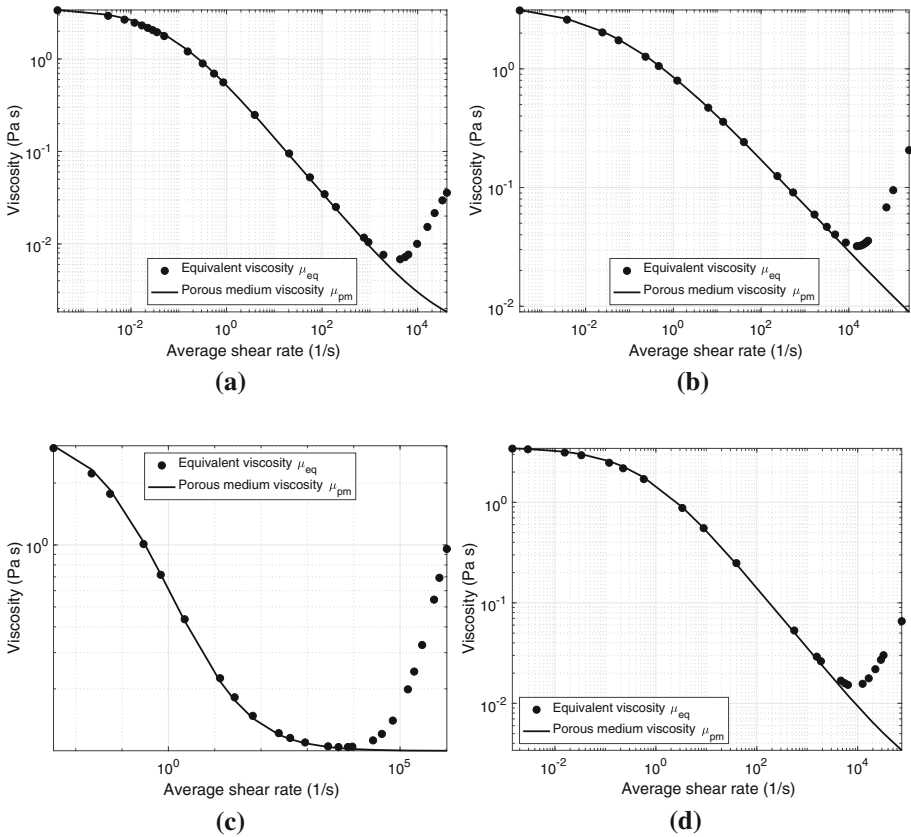
Fig. 7 μ_{eq} and μ_{pm} versus $\dot{\gamma}$ curves. **a** Shear-thinning fluid #1, **b** Shear-thinning fluid #2, **c** Shear-thinning fluid #3, **d** Shear-thinning fluid #4

$$\beta \rho K \frac{Q}{A} = \beta \rho K^{3/2} \frac{Q/A}{\sqrt{K}} = \beta \rho K^{3/2} \frac{|v|}{\sqrt{K\phi}} = \beta \rho K^{3/2} \dot{\gamma} \qquad (20)$$

Therefore, at very high flow rate, the inertial term dominates in Eq. (10) and the μ_{eq} versus $\dot{\gamma}$ curves should become a straight line and its slope is $\beta \rho K^{3/2}$. Indeed, in Fig. 9a, all the curves including both Newtonian fluids and shear-thinning fluids collapse onto the same red dashed straight line, which agrees very well with literature finding that the inertial coefficient β is only dependent on the porous medium geometry. The slope of the red dashed straight line in Fig. 9a is $\beta \rho K^{3/2}$, and the value of β is the average value of six fitted β values in Table 3. As shown in Fig. 9b, for Newtonian fluids flow in the rough fracture, when the average shear rate is small (or the flow rate is low), the dimensionless equivalent viscosity μ_{eq}/μ_0 is equal to one since the flow is linear and the equivalent viscosity equals to the constant Newtonian viscosity. When the average shear rate is high, the inertial force can no longer be ignored compared with the viscous force and then the dimensionless equivalent viscosity will increase and could be as high as 10. For shear-thinning fluids, at low flow rate, the dimensionless equivalent viscosity decreases as the average shear rate increases only due to the shear-thinning effect of the fluid rheology. At the strong inertial regime, the dimensionless equivalent viscosity will increase mainly due to the inertial forces. However,

$\textcircled{\tiny 2}$ Springer
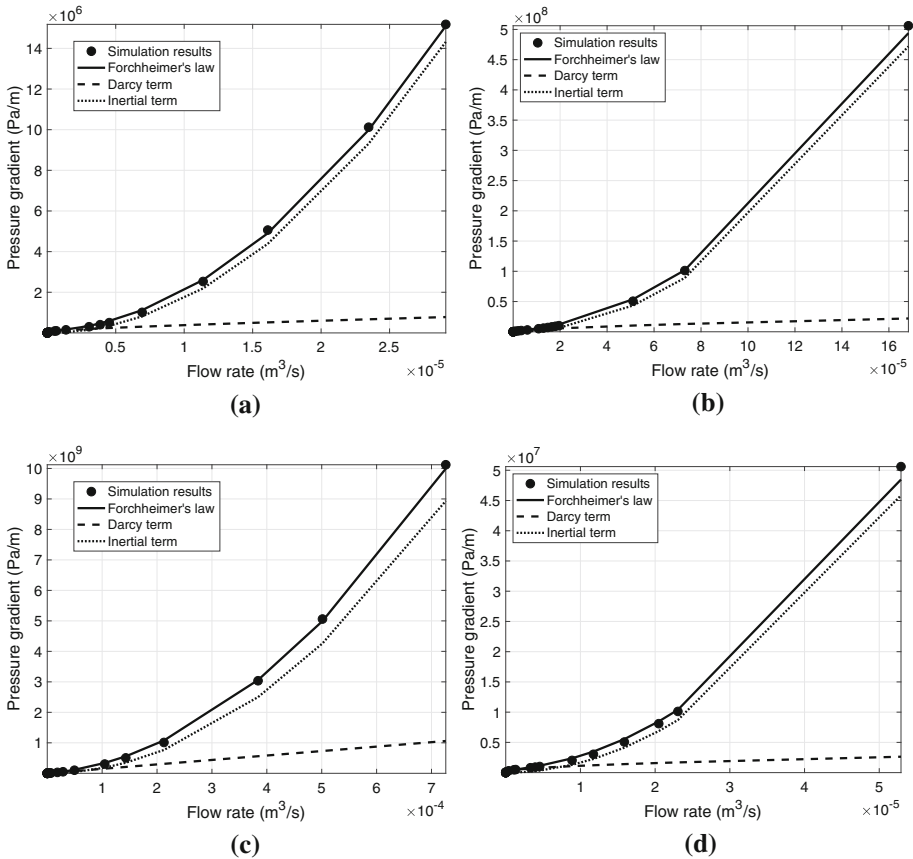
Fig. 8 Pressure gradient versus flow rate curves for shear-thinning fluids flow in the rough fracture. **a** Shear-thinning fluid #1, **b** Shear-thinning fluid #2, **c** Shear-thinning fluid #3, **d** Shear-thinning fluid #4. Symbols represent microscale simulation results. Solid line is the fitted Forchheimer's equation. Dot-dashed and dashed lines are the inertial term and Darcy term in Forchheimer's equation, respectively. The growing discrepancy between "Simulation results" (matching very well with the fitted "Forchheimer's law") and "Darcy term" shows that the inertial pressure losses are becoming dominating with the increase in flow rate

in our simulations (the largest Reynolds number could approach about 1000), the equivalent viscosity of the shear-thinning fluid could not increase to the initial upper Newtonian viscosity plateau and the dimensionless equivalent viscosity is always smaller than one as shown in Fig. 9b.

At low flow rate (low Re), ΔP_{shear} is dominant and the linear Darcy's law is applicable. When the flow rate is very high (high Re), $\Delta P_{inertial}$ can no longer be ignored compared to ΔP_{shear} and the linear Darcy's law is inadequate. Based on the definition of Re_c in Sect. 2.1 (Eq. (12)), the calculated Re_c for six sets of simulations is given in Table 3. The results show that six Re_c values are approximately the same (the standard deviation of these six Re_c values is 0.036), which means that the critical Reynolds number Re_c is only a function of porous medium geometry and in our case has no obvious dependence on the fluid properties.
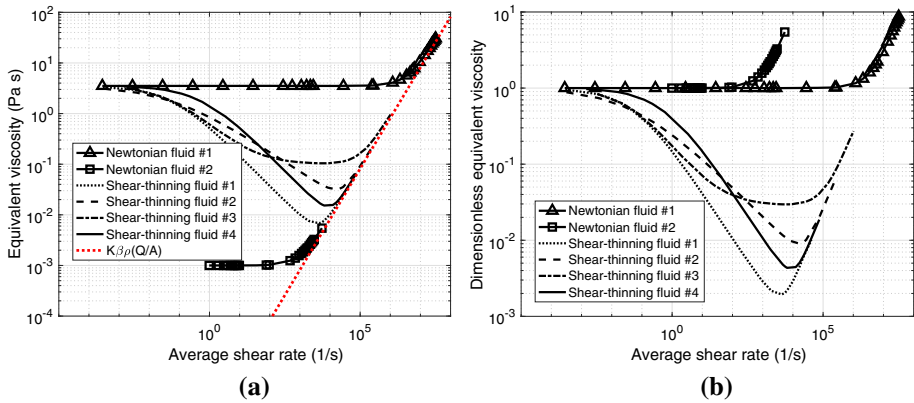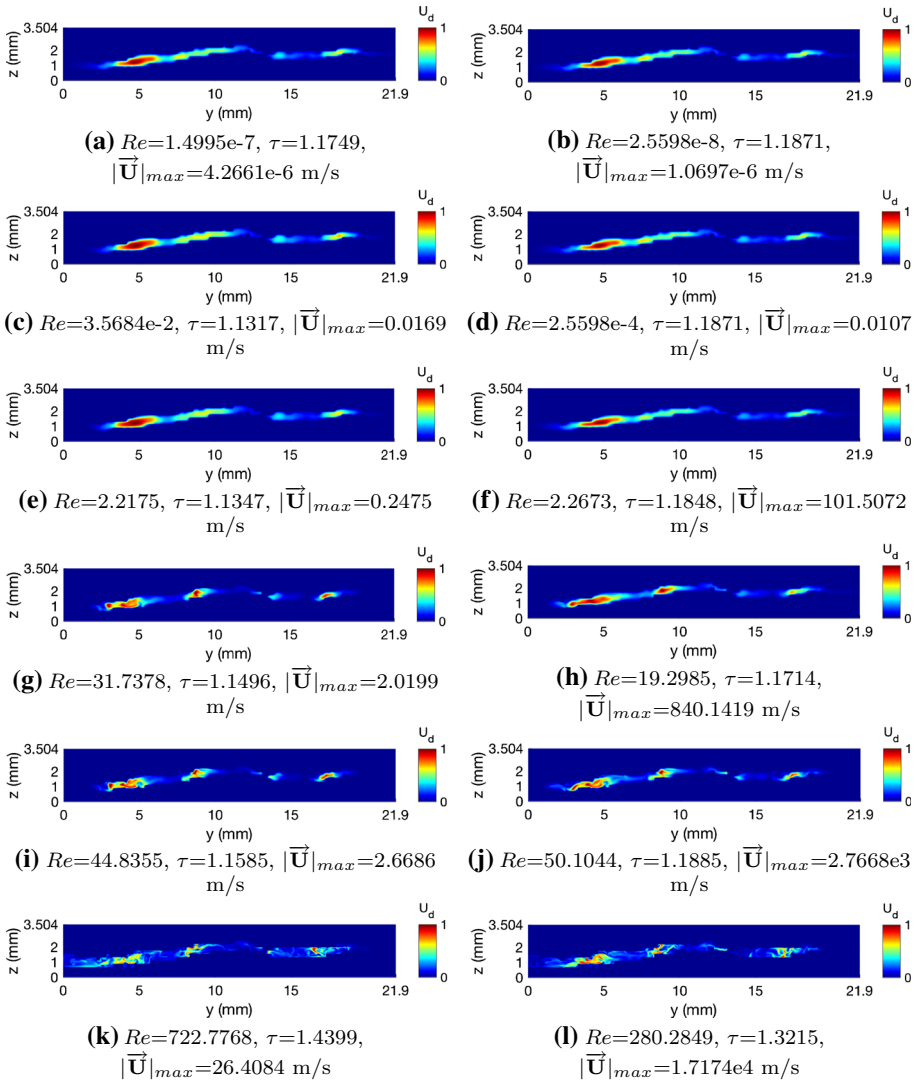
Fig. 9 Comparison of equivalent viscosity between the two Newtonian fluids and four shear-thinning fluids. μ_{eq} is calculated from the microscale flow simulation results based on Eq. (9). **a** μ_{eq} versus $\dot{\gamma}$ curves, **b** μ_{eq}/μ_0 (dimensionless equivalent viscosity) versus $\dot{\gamma}$ curves. For shear-thinning fluids, μ_0 represents the initial viscosity or upper Newtonian plateau. For Newtonian fluids, μ_0 represents the constant Newtonian viscosity and the "pseudo"-increase in μ_{eq} is because of the inertial effects. The slope of the red dashed straight line in **a** is $\beta \rho K^{3/2}$, and the value of β is the mean value of six fitted β values in Table 3. Specifically, the mean for fitted β is 903 and the standard deviation value is 15.39

3.2 Microscopic Flow Patterns

In Sect. 3.1, a number of macroscopic relationships have been studied, including the pressure drop-flow rate curves, equivalent/apparent viscosity curves and critical Reynolds number. In this section, we mainly focus on the quantification of flow details of the microscale simulations and to give insight of the underlying physical nature for the observed macroscopic flow behavior.

Orthogonal views in Fig. 2 show the tortuosity of the fracture space that is impossible to gauge from aperture field, but is obviously affecting flow patterns seen in an individual cross-section (Fig. 10). As shown in Fig. 2, YZ cross-section shows a connected fracture space; however, the fracture space in the XY mid-plane is not connected and XZ plane shows that it meanders both above and below the XY mid-plane. Thus even though a portion of the space might appear relatively wide in YZ cross-section, just before it there might have been solid space that is blocking the flow.

One specific advantage of microscale flow simulation is that it could provide the detailed flow information in the porous media. Figure 10 shows the dimensionless velocity magnitude fields for both shear-thinning fluid #1 and Newtonian fluid #1 across the slice $x = 1012$ under different Reynolds numbers. We can see that, although the open fracture runs through the whole slice $x = 1012$ (as shown in the YZ view of Fig. 2), the fluid mainly flows through a certain part of the fracture. As shown in Fig. 10, the fluids do not access the left open fracture part (upper part of the YZ view in Fig. 2 indicated with a red ellipse) at all except for the cases where Reynolds number are very large (Fig. 10k, l). This is because the flow field is determined by the overall aperture field distributions. Specifically, as shown in the aperture field (Fig. 1), just before the slice $x=1012$, in the upper part, there are some darker areas where the aperture is very small (even with zero aperture). In addition, we can also see the isolated fracture space around slice $x=1012$ from the XZ view of Fig. 2. Therefore, the fluid can hardly access the left open fracture part of slice $x=1012$ even though its aperture is very large (as shown in the YZ view of Fig. 2 indicated with a red ellipse).

(a) $Re=1.4995e-7$, $\tau=1.1749$, $|\vec{\mathbf{U}}|_{max}=4.2661e-6$ m/s

(b) $Re=2.5598e-8$, $\tau=1.1871$, $|\vec{\mathbf{U}}|_{max}=1.0697e-6$ m/s

(c) $Re=3.5684e-2$, $\tau=1.1317$, $|\vec{\mathbf{U}}|_{max}=0.0169$ m/s

(d) $Re=2.5598e-4$, $\tau=1.1871$, $|\vec{\mathbf{U}}|_{max}=0.0107$ m/s

(e) $Re=2.2175$, $\tau=1.1347$, $|\vec{\mathbf{U}}|_{max}=0.2475$ m/s

(f) $Re=2.2673$, $\tau=1.1848$, $|\vec{\mathbf{U}}|_{max}=101.5072$ m/s

(g) $Re=31.7378$, $\tau=1.1496$, $|\vec{\mathbf{U}}|_{max}=2.0199$ m/s

(h) $Re=19.2985$, $\tau=1.1714$, $|\vec{\mathbf{U}}|_{max}=840.1419$ m/s

(i) $Re=44.8355$, $\tau=1.1585$, $|\vec{\mathbf{U}}|_{max}=2.6686$ m/s

(j) $Re=50.1044$, $\tau=1.1885$, $|\vec{\mathbf{U}}|_{max}=2.7668e3$ m/s

(k) $Re=722.7768$, $\tau=1.4399$, $|\vec{\mathbf{U}}|_{max}=26.4084$ m/s

**(l)** $Re=280.2849$, $\tau=1.3215$, $|\vec{\mathbf{U}}|_{max}=1.7174e4$ m/s

Fig. 10 Dimensionless velocity magnitude fields across the slice $x=1012$ (whose geometry is shown in the YZ view of Fig. 2) for both shear-thinning fluid #1 (left column) and Newtonian fluid #1 (right column)

To quantify the velocity distribution in the whole fracture, tortuosity is used in the following analysis. There are many different definitions of tortuosity (Ghanbarian et al. 2013), and here we adopt the following definition from (Duda et al. 2011; Zhao et al. 2018):

$$\tau = \frac{\overline{|\mathbf{U}|}}{\overline{U_x}} = \frac{\overline{\sqrt{U_x^2 + U_y^2 + U_z^2}}}{\overline{U_x}} \tag{21}$$

where $\overline{|\mathbf{U}|}$ and $\overline{U_x}$ are the average values of velocity magnitude and x-component velocity, respectively. These information can be obtained from the microscale velocity distributions.
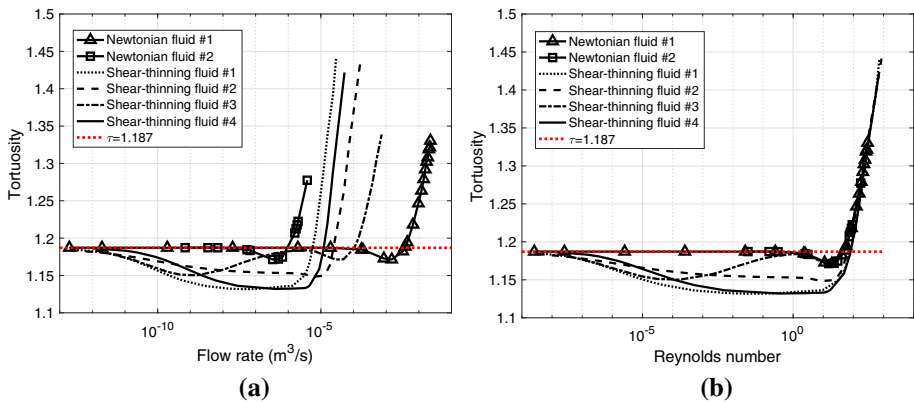
Fig. 11 Comparison of tortuosity curves between Newtonian fluids and shear-thinning fluids in the rough fracture. **a** Tortuosity versus flow rate curves. **b** Tortuosity versus Reynolds number curves

The variation of tortuosity curves for both Newtonian and shear-thinning fluids is shown in Fig. 11. With the increase in flow rate (Fig. 11a) or Reynolds number (Fig. 11b), for both two Newtonian fluids, the tortuosity remains constant (1.187) at first, then at some point decreases, and finally increases. Similar phenomenon has been observed in previous studies (Agnaou et al. 2017; Sivanesapillai et al. 2014). Agnaou et al. (2017) did a thorough microscopic Newtonian fluid flow analysis on two dimensional model structures to investigate the origin of the inertial deviation from Darcy's law. For all the six different configurations, they found that the tortuosity remains constant in the linear flow regime and weak inertial regime, and then a well-defined decrease in tortuosity can be observed at the beginning of the transition from weak inertial to the strong inertial (also called Forchheimer) regime. Since the Berea fracture, which could be viewed as a very complex heterogeneous assembly of the simplified model structures, is much more complicated than 2D model structures, the transitions from linear flow regime to weak inertial regime and from weak to strong inertial regime, and also beyond the strong inertial regime can not be identified very clearly from Fig. 11. In addition, if the special fluid rheology of shear-thinning fluids comes into play, the behind physical mechanisms and induced microscopic flow behaviors would be more complicated further. Therefore, in this work, firstly, a brief analysis of the above tortuosity trend for Newtonian fluids will be discussed and for more details the reader could refer to Agnaou et al. (2017) and Sivanesapillai et al. (2014). After that, combined with the dimensionless velocity magnitude fields shown in Fig. 10 and the comparison with Newtonian fluids, a detailed microscopic analysis of the Shear-thinning fluids flow behavior will be discussed.

To discuss the reasons why the tortuosity of Newtonian fluids decreases first and then increases, the comparison between tortuosity curves and dimensionless equivalent viscosity curves of two Newtonian fluids is shown in Fig. 12. From Fig. 12, we can see that when Reynolds number is smaller than about 0.28, the equivalent viscosity remains constant and is equal to the constant Newtonian viscosity (since the dimensionless equivalent viscosity keeps to be 1), and the tortuosity also remains to be the constant Newtonian tortuosity (1.187). In this condition, the fluid flow is dominated by the viscous force and is in the creeping flow regime or weak initial regime. The streamlines remain constant and therefore the dimensionless velocity magnitude distributions remain almost the same, as shown in Fig. 10b, d. Then, with the increase in flow rate or Reynolds number, the effect of inertial forces increases and the fluid flow becomes more channelized because of both the pore geometry and the shape

Fig. 12 Comparison of tortuosity curves and dimensionless equivalent viscosity curves of two sets of Newtonian fluids simulations
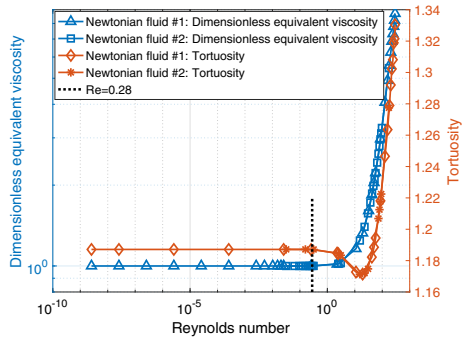
change of the eddies, which can be reflected from both Fig. 10f, h, whose red areas indicate higher velocity increase compared with Fig. 10b, d. Accordingly, the tortuosity decreases, which indicates the beginning of the transition from weak inertial to the Forchheimer regime according to Agnaou et al. (2017) and Sivanesapillai et al. (2014). With further increase in flow rate or Reynolds number, the inertial forces would dominate the flow and the streamlines become more and more unstable even turbulent, as shown in Fig. 10j, l. This will cause a sharp increase in both the tortuosity and the fluid flow resistances. As a result, the dimensionless equivalent viscosity increases sharply as shown in Fig. 12.

For shear-thinning fluids, we take the shear-thinning fluid #1 as an example to analyze the detailed flow behavior. When the flow rate is very low (Re is very small), the dimensionless velocity magnitude distribution of the shear-thinning fluid is similar to that of Newtonian fluid, as shown in Fig. 10a, b. However, even in the linear flow regime (at low flow rate) the tortuosity of shear-thinning fluids decreases with the increase in flow rate. This is because the so-called channelization phenomenon is more pronounced for shear-thinning fluids. For Newtonian fluids, the fluid velocity is usually larger in the position with a larger local aperture and vice versa, which is the so-called fluid channelization phenomenon. This will induce a larger shear rate, and in case of a shear-thinning fluid a smaller viscosity, in larger apertures. Therefore, the shear-thinning fluids will have smaller viscosities in larger apertures compared with those in smaller apertures, which in turn increases the velocity in larger apertures further. As a result, the shear-thinning fluids would have a more pronounced channelization effect and the tortuosity is smaller than that of Newtonian fluids under the same order of Re as shown in Fig. 10e, f (or c, d), where (e) has a larger and darker red area than (f) since (e) has a more pronounced channelization effect, and therefore the shear-thinning fluid has a smaller tortuosity. In addition, with the increase in flow rate or Reynolds number, the channelization of shear-thinning fluid becomes more significant. As shown in Fig. 10c, the red areas with high velocity increase compared with those in Fig. 10a. Therefore, as shown in Fig. 11, in the initial period, the tortuosity of shear-thinning fluids decreases with the increase in flow rate (or Reynolds number).

For shear-thinning fluids, the increase in tortuosity could be caused by two effects: the lower Newtonian viscosity plateau and the inertial forces coming into play at high flow rate and becoming dominant at very high flow rate. Under the influences of shear-thinning effect, the lower Newtonian viscosity plateau, inertial forces, and especially the complicated fracture geometry, the dimensionless velocity distribution under $Re = 2.2175$ is similar to that under $Re = 3.5684e - 2$, as shown in Fig. 10c, e. Therefore, the tortuosity of Shear-thinning fluid #1 shown in Fig. 11b has no obvious change from $Re = 1e - 2$ to $Re \approx 3$. Thereafter, with further increase in flow rate or Reynolds number, the effect of inertial forces increases, and

the complicated fracture rough surfaces come into play, then the flow field becomes unstable even turbulent as shown in Fig. 10g,i, k, causing an obvious increase in the tortuosity, which is the same trend as the Newtonian fluids.

Specifically, for shear-thinning fluids, the increase in tortuosity caused by the lower Newtonian viscosity plateau could be shown very clearly by the tortuosity curve of Shear-thinning fluid #3 in Fig. 11. Compared with the Newtonian fluids, its tortuosity will first decrease due to the shear-thinning effect. According to Table 2, the lower Newtonian viscosity plateau of Shear-thinning fluid #3 is larger than the other three cases and it means its viscosity would decrease to this lower limit value earlier than the other three shear-thinning fluids. After approaching the lower Newtonian viscosity plateau, it will behave like a Newtonian fluid and therefore its tortuosity will increase to the constant Newtonian tortuosity value (1.187). After that, it will have exactly the same behavior as the Newtonian fluids (as shown very clearly in Fig. 11b).

4 Discussion: Correlation of Shift Factor for Shear-Thinning Fluids Flow in the Rough Fracture

For practical applications, the relationship between pressure drop and flow rate for shear-thinning fluid flow through the rough fracture is very important for higher-level hydraulic fracturing and reservoir simulators. According to Eq. (4), to obtain the pressure drop–flow rate relationship for shear-thinning fluid flow through a rough fracture, μ_{pm} should be known. To calculate μ_{pm} based on Eq. (6), $\dot{\gamma}_{pm}$ should be known. Therefore, according to Eq. (7), the correlation of shift factor α for shear-thinning fluid flow through a rough fracture is necessary to obtain the pressure drop-flow rate relationship. Because shift factor α is a function of both fluid rheology property and the porous medium geometry and is influenced by a lot of parameters, there have not been satisfying correlations for it in the literature.

According to Table 1, we can see that for simple power-law fluid flow in a narrow slit model, the shift factor α is a function of power-law index n and there is no geometry parameter in this shift factor α formula. However, for Cross power-law fluid flow in a narrow slit model, even though we can obtain the semi-analytical flow rate value at a specific pressure gradient as shown in Sect. 2.3, the analytical shift factor α formula cannot be derived due to the more complex fluid rheology constitutive model of Cross power-law fluid compared with the simplest power-law fluid rheology model. Since the $(\dot{\gamma}, \mu_{eq})$ data could be obtained from the semi-analytical solution of Cross power-law fluid flow in a narrow slit model, we could use the same procedure described in Sect. 3.1.2 to obtain the shift factor α_{slit} for all the four sets of shear-thinning fluids as shown in Table 3. We also simulated several cases of Cross power-law fluid flow in a narrow slit with different apertures for each set of fluid rheology properties. These simulations are not shown here. Our fitting results show that α_{slit} is only dependent on the fluid rheology property and not influenced by the slit geometry, i.e., its aperture.

The comparison between the shear-thinning fluid flow in a rough fracture and that in a narrow slit model shows that the substantial difference is the fracture rough surfaces. The rough surfaces will cause the bending of the streamlines, which can be characterized by the fluid flow tortuosity. Therefore, we introduce tortuosity into the correlation of shift factor α. Our proposed correlation of shift factor α for shear-thinning fluids flow in the rough fracture is as follows:

$$\alpha = \alpha_{slit}\tau = f(n)\tau \tag{22}$$
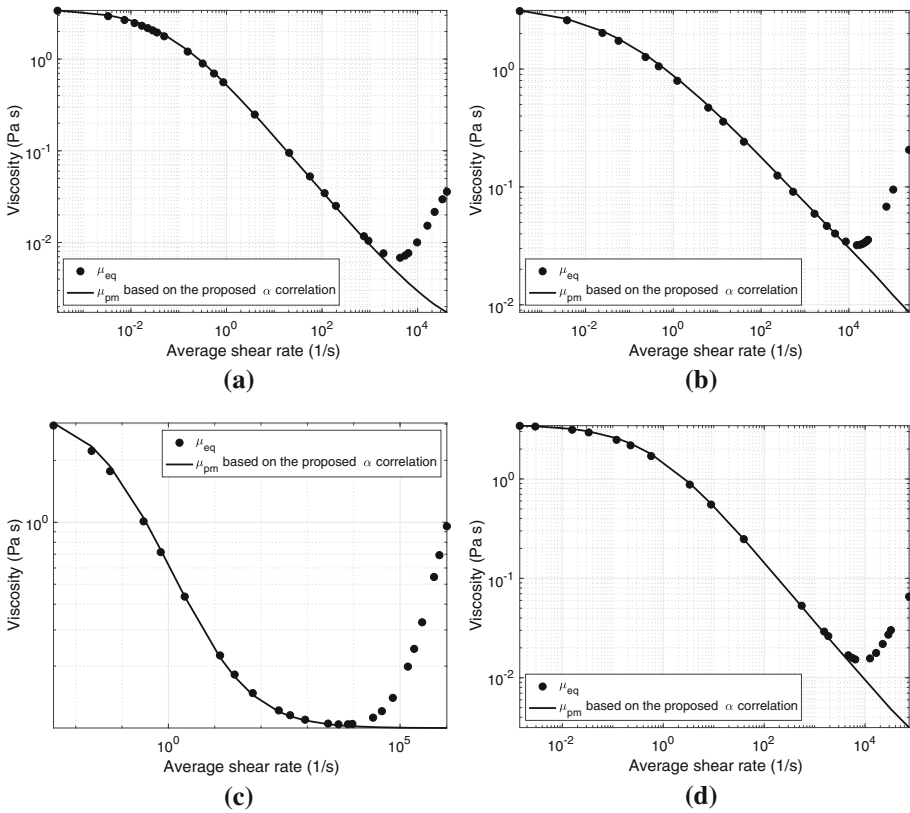
Fig. 13 μ_{eq} and correlated μ_{pm} versus $\dot{\gamma}$ curves. **a** Shear-thinning fluid #1, **b** Shear-thinning fluid #2, **c** Shear-thinning fluid #3, **d** Shear-thinning fluid #4. μ_{pm} is calculated with the proposed shift factor α correlation (Eq. (22)) based on Eq. (6)

where α_{slit} (or $f(n)$) is the shift factor for the same shear-thinning fluid flow in a narrow slit model. Specifically, for the simplest power-law fluid rheology model, we can have the analytical formula for α_{slit} as shown in Table 1. But for more complex fluid rheology models such as the Cross power-law fluid rheology model used in this work, the analytical formula for α_{slit} could not be derived based on the classical fluid dynamic theory and α_{slit} can be obtained by least square method fitting to the semi-analytical $(\dot{\gamma}, \mu_{\text{eq}})$ data. The tortuosity τ here is the values in Sect. 3.2 directly calculated from microscale fluid flow velocity profile based on Eq. (21).

With our correlation of shift factor α (Eq. (22)), the calculated porous medium viscosity μ_{pm} based on Eq. (6) is compared with the equivalent viscosity μ_{eq} calculated from the microscale simulation results based on Eq. (9) for four sets of shear-thinning fluids flow in the rough fracture. Figure 13 shows that for all the four sets of shear-thinning fluids, our correlation for shift factor α works very well.

We further attempt to predict shift factor α without doing any microscale flow simulations. With that in mind, we propose the shift factor α correlation (Eq. (22)) in the following form:

$$\alpha = \alpha_{\text{slit}} \tau_{\text{geometric}} = f(n) \tau_{\text{geometric}} \tag{23}$$

where $\tau_{\text{geometric}}$ is the geometric tortuosity which could be obtained from image analysis without doing any microscale flow simulations. It means that $\alpha/\alpha_{\text{slit}}$ should be approximately the geometric tortuosity $\tau_{\text{geometric}}$ of our rough fracture. Note that $\tau_{\text{geometric}} = \langle L_g \rangle / L_s$ is defined as the average length $\langle L_g \rangle$ of the paths through the porous medium/fracture, divided by the length of the sample L_s. Tokan-Lawal (2015) used medial axis analysis to obtain $\langle L_g \rangle$ and found $\tau_{\text{geometric}}$ to be 1.3 for this Berea fracture (see Fig. 6.21 in Tokan-Lawal (2015)). Tokan-Lawal et al. (2015) performed the same analysis in other rough fractures. According to our microscale simulations of four sets of shear-thinning fluids flow in the rough fracture, the $\alpha/\alpha_{\text{slit}}$ values are given in Table 3, and we can see that they are roughly the geometric tortuosity.

5 Summary and Conclusions

In this work, for the first time, a fully-3D microscale flow simulation for shear-thinning fluids in a realistic rough fracture is conducted. The simulation details allow analysis of both microscopic and macroscopic flow parameters. Our main findings are as follows.

1. We confirm the previous conclusion in the literature that the non-Darcian Forchheimer's law could be extended to the shear-thinning fluids flow in porous media.
2. Both the inertial coefficient β in Forchheimer's equation and the critical Reynolds number Re_c only depend on the fracture geometry and have no obvious dependence on the fluid rheology property.
3. We propose a new correlation of shift factor α for shear-thinning fluid flow in a rough fracture (see Eq. (22)). It is quantified by the product of $f(n)$ (or α_{slit}) and the tortuosity. $f(n)$ could be obtained from the analytical/semi-analytical solutions of the same shear-thinning fluid flow in a smooth narrow slit model. Two approaches are provided for the tortuosity quantification. One is based on the detailed microscale fluid velocity field and produces a very accurate shift factor α which is changing with the pressure gradient. The other is the geometric tortuosity $\tau_{\text{geometric}}$ obtained by image analysis without doing any microscale simulations, which provides an approximate value for shift factor α.

In addition, the macroscopic pressure drop-flow rate laws, including both the Darcy's and non-Darcian laws, incorporated with the newly proposed shift factor α correlation could be used into the higher-level simulators to instruct the related industrial applications.

Further steps of this work include (1) the validation of the proposed shift factor α correlation for other non-Newtonian fluids (such as Carreau and yield-stress fluids) and other realistic rough fractures, (2) the investigation of shear-thinning fluid flow behavior in the rough fracture when considering the fluid leak-off and also (3) the incorporation of particulate transport into the microscale fluid flow simulation which also has wide industrial applications.

Finally, even though Sect. 3.2 gives some insights of the underlying physical nature of this complicated flow characteristics for shear-thinning fluids through a realistic rough fracture, such as the flow behavior transition from viscous force dominated flow to inertial force dominated flow under the influence of both fluid rheology and porous medium geometry, the complete physical origins of these flow regime transitions for non-Newtonian fluids still need to be understood by theory or further simulations, for example, via the promising microscale simulation approaches such as CFD and LBM, and starting from very simple geometries. The authors are actively working on this problem.

Appendix A: Derivation of Shift Factor α for Two Simple Cases Based on the Classical Fluid Mechanics/Dynamics Theory

A.1 Simple Power-Law Fluid in a Tube

Refer to Eq. (8.3–9) in Bird et al. (2002) (Revised Second Edition) for the average velocity which is obtained by dividing the total volumetric flow rate by the cross-sectional area,

$$\langle v_z \rangle = \frac{R}{\frac{1}{n}+3}\left(\frac{\Delta P R}{2K'L}\right)^{\frac{1}{n}} = \frac{K}{\mu_{\text{eq}}}\frac{\Delta P}{L} = \frac{\frac{R^2}{8}}{\mu_{\text{eq}}}\frac{\Delta P}{L}$$

where R is the tube radius [L].

$$\mu_{\text{eq}} = \frac{R^2}{8}\frac{\Delta P}{L}\frac{\frac{1}{n}+3}{R}\left(\frac{\Delta P R}{2K'L}\right)^{-\frac{1}{n}} = \frac{\Delta P R}{2L}\frac{3n+1}{4n}\left(\frac{\Delta P R}{2K'L}\right)^{-\frac{1}{n}}$$

$$\frac{\mu_{\text{eq}}}{K'} = \frac{\Delta P R}{2K'L}\frac{3n+1}{4n}\left(\frac{\Delta P R}{2K'L}\right)^{-\frac{1}{n}} = \frac{3n+1}{4n}\left(\frac{\Delta P R}{2K'L}\right)^{\frac{n-1}{n}}$$

Average shear rate for a tube:

$$\dot{\gamma} = \frac{\langle v_z \rangle}{\sqrt{K\phi}} = \frac{\langle v_z \rangle}{\sqrt{K}} = \frac{\frac{R}{\frac{1}{n}+3}\left(\frac{\Delta P R}{2K'L}\right)^{\frac{1}{n}}}{\frac{R}{\sqrt{8}}} = \frac{\sqrt{8}}{\frac{1}{n}+3}\left(\frac{\Delta P R}{2K'L}\right)^{\frac{1}{n}}$$

According to $\frac{\mu_{\text{eq}}}{K'} = \frac{\mu_{\text{pm}}}{K'} = \left(\dot{\gamma}_{\text{pm}}\right)^{n-1} = \left(\alpha\dot{\gamma}\right)^{n-1}$, which is valid only in linear flow regime, we can get

$$\frac{3n+1}{4n}\left(\frac{\Delta P R}{2K'L}\right)^{\frac{n-1}{n}} = \left(\alpha\frac{\sqrt{8}}{\frac{1}{n}+3}\left(\frac{\Delta P R}{2K'L}\right)^{\frac{1}{n}}\right)^{n-1} = \left(\alpha\frac{\sqrt{8}}{\frac{1}{n}+3}\right)^{n-1}\left(\frac{\Delta P R}{2K'L}\right)^{\frac{n-1}{n}}$$

$$\left(\alpha\frac{\sqrt{8}}{\frac{1}{n}+3}\right)^{n-1} = \frac{3n+1}{4n}$$

Therefore, the shift factor α in the case of the simple power-law fluid flow in a tube is:

$$\alpha_{tube} = \frac{3n+1}{\sqrt{8}n}\left(\frac{3n+1}{4n}\right)^{\frac{1}{n-1}} = \sqrt{2}\left(\frac{3n+1}{4n}\right)^{\frac{n}{n-1}}$$

A.2 Simple Power-Law Fluid in a Narrow Slit

Refer to Eq. (8.3–14) in Bird et al. (2002) (Revised Second Edition) for the average velocity,

$$\langle v_z \rangle = \frac{B}{\frac{1}{n}+2}\left(\frac{\Delta P B}{K'L}\right)^{\frac{1}{n}} = \frac{K}{\mu_{\text{eq}}}\frac{\Delta P}{L} = \frac{\frac{(2B)^2}{12}}{\mu_{\text{eq}}}\frac{\Delta P}{L}$$

where B is the half-width of the narrow slit [L].

$$\mu_{\text{eq}} = \frac{(2B)^2}{12} \frac{\Delta P}{L} \frac{\frac{1}{n}+2}{B} \left(\frac{\Delta P B}{K'L}\right)^{-\frac{1}{n}} = \frac{2n+1}{3n} \frac{\Delta P B}{L} \left(\frac{\Delta P B}{K'L}\right)^{-\frac{1}{n}}$$

$$\frac{\mu_{\text{eq}}}{K'} = \frac{2n+1}{3n} \frac{\Delta P B}{K'L} \left(\frac{\Delta P B}{K'L}\right)^{-\frac{1}{n}} = \frac{2n+1}{3n} \left(\frac{\Delta P B}{K'L}\right)^{\frac{n-1}{n}}$$

Average shear rate for a narrow slit:

$$\dot{\gamma} = \frac{\langle v_z \rangle}{\sqrt{K\phi}} = \frac{\langle v_z \rangle}{\sqrt{K}} = \frac{\langle v_z \rangle}{\sqrt{\frac{(2B)^2}{12}}} = \frac{\sqrt{3}}{B} \frac{B}{\frac{1}{n}+2} \left(\frac{\Delta P B}{K'L}\right)^{\frac{1}{n}} = \frac{\sqrt{3}n}{2n+1} \left(\frac{\Delta P B}{K'L}\right)^{\frac{1}{n}}$$

According to $\frac{\mu_{\text{eq}}}{K'} = \frac{\mu_{\text{pm}}}{K'} = \left(\dot{\gamma}_{\text{pm}}\right)^{n-1} = \left(\alpha\dot{\gamma}\right)^{n-1}$, we can get

$$\frac{2n+1}{3n} \left(\frac{\Delta P B}{K'L}\right)^{\frac{n-1}{n}} = \left(\alpha \frac{\sqrt{3}n}{2n+1} \left(\frac{\Delta P B}{K'L}\right)^{\frac{1}{n}}\right)^{n-1}$$

$$\frac{2n+1}{3n} = \left(\alpha \frac{\sqrt{3}n}{2n+1}\right)^{n-1}$$

Therefore, the shift factor α in the case of the simple power-law fluid flow in a narrow slit is:

$$\alpha_{\text{slit}} = \left(\frac{2n+1}{3n}\right)^{\frac{1}{n-1}} \frac{2n+1}{\sqrt{3}n} = \sqrt{3} \left(\frac{2n+1}{3n}\right)^{\frac{n}{n-1}}$$

References

Agnaou, M., Lasseux, D., Ahmadi, A.: Origin of the inertial deviation from Darcy's law: an investigation from a microscopic flow analysis on two-dimensional model structures. Phys. Rev. E **96**(4), 043105 (2017)

Balhoff, M., Sanchez-Rivera, D., Kwok, A., Mehmani, Y., Prodanović, M.: Numerical algorithms for network modeling of yield stress and other non-Newtonian fluids in porous media. Transp. Porous Media **93**(3), 363–379 (2012). https://doi.org/10.1007/s11242-012-9956-5

Bird, RB., Armstrong, R.C., Hassager, O.: Dynamics of Polymeric Liquids, Volume 1: Fluid Mechanics, 2nd Edition (1987)

Bird, RB., Stewart, W.E., Lightfoot, E.N.: Transport Phenomena, Revised 2nd Edition (2002)

Briggs, S., Karney, B.W., Sleep, B.E.: Numerical modeling of the effects of roughness on flow and eddy formation in fractures. J. Rock Mech. Geotech. Eng. **9**(1), 105–115 (2017). https://doi.org/10.1016/j.jrmge.2016.08.004

Brush, D.J., Thomson, N.R.: Fluid flow in synthetic rough-walled fractures: Navier–Stokes, Stokes, and local cubic law simulations. Water Resour. Res. **39**(4), 1085 (2003). https://doi.org/10.1029/2002WR001346

Cardenas, M.B., Slottke, D.T., Ketcham, R.A., Sharp, J.M.: Effects of inertia and directionality on flow and transport in a rough asymmetric fracture. J. Geophys. Res.: Solid Earth 114(B6) (2009). https://doi.org/10.1029/2009JB006336

Chauveteau, G.: Rodlike polymer solution flow through fine pores: influence of pore size on rheological behavior. J. Rheol. **26**(2), 111–142 (1982). https://doi.org/10.1122/1.549660

Christopher, R.H., Middleman, S.: Power-law flow through a packed tube. Ind. Eng. Chem. Fundam. **4**(4), 422–426 (1965). https://doi.org/10.1021/i160016a011

Ciriello, V., Longo, S., Chiapponi, L., Di Federico, V.: Porous gravity currents: a survey to determine the joint influence of fluid rheology and variations of medium properties. Adv. Water Resour. **92**, 105–115 (2016). https://doi.org/10.1016/j.advwatres.2016.03.021

Comba, S., Dalmazzo, D., Santagata, E., Sethi, R.: Rheological characterization of xanthan suspensions of nanoscale iron for injection in porous media. J. Hazard. Mater. **185**(2), 598–605 (2011). https://doi.org/10.1016/j.jhazmat.2010.09.060

Crandall, D., Bromhal, G., Karpyn, Z.T.: Numerical simulations examining the relationship between wall-roughness and fluid flow in rock fractures. Int. J. Rock Mech. Min. Sci. **47**(5), 784–796 (2010)

Dharmawan, I.A., Ulhag, R.Z., Endyana, C., Aufaristama, M.: Numerical simulation of non-Newtonian fluid flows through fracture network. In: IOP conference series: earth and environmental science **29**, 012–030 (2016). https://doi.org/10.1088/1755-1315/29/1/012030

Di Federico, V.: Non-Newtonian flow in a variable aperture fracture. Transp. Porous Media **30**(1), 75–86 (1998). https://doi.org/10.1023/A:1006512822518

Di Federico, V.: On non-Newtonian fluid flow in rough fractures. Water Resour. Res. **37**(9), 2425–2430 (2001). https://doi.org/10.1029/2001WR000359

Di Federico, V., Longo, S., King, S.E., Chiapponi, L., Petrolo, D., Ciriello, V.: Gravity-driven flow of Herschel–Bulkley fluid in a fracture and in a 2d porous medium. J. Fluid Mech. **821**, 59–84 (2017). https://doi.org/10.1017/jfm.2017.234

Duda, A., Koza, Z., Matyka, M.: Hydraulic tortuosity in arbitrary porous media flow. Phys. Rev. E **84**(3), 036–319 (2011). https://doi.org/10.1103/PhysRevE.84.036319

Felisa, G., Ciriello, V., Longo, S., Di Federico, V.: A simplified model to evaluate the effect of fluid rheology on non-Newtonian flow in variable aperture fractures. In: 19th EGU General Assembly, EGU2017, Proceedings from the Conference Held 23–28 April, 2017 in Vienna, Austria, vol. 19 (2017)

Feng, Y., Gray, K.E.: Modeling lost circulation through drilling-induced fractures. SPE J. (2017a). https://doi.org/10.2118/187945-PA

Feng, Y., Gray, K.E.: Review of fundamental studies on lost circulation and wellbore strengthening. J. Pet. Sci. Eng. **152**, 511–522 (2017b). https://doi.org/10.1016/j.petrol.2017.01.052

Feng, Y., Jones, J.F., Gray, K.E.: A review on fracture-initiation and -propagation pressures for lost circulation and wellbore strengthening. SPE Drill. Complet. **31**(02), 134–144 (2016). https://doi.org/10.2118/181747-PA

Forchheimer, P.: Wasserbewegung durch boden. Zeitschrift des Vereins deutscher Ingenieure **45**(50), 1782–1788 (1901)

Ge, S.: A governing equation for fluid flow in rough fractures. Water Resour. Res. **33**(1), 53–61 (1997). https://doi.org/10.1029/96WR02588

Ghanbarian, B., Hunt, A.G., Ewing, R.P., Sahimi, M.: Tortuosity in porous media: a critical review. Soil Sci. Soc. Am. J. **77**(5), 1461–1477 (2013). https://doi.org/10.2136/sssaj2012.0435

Hawkes, C.D., McLellan, P.J., Zimmer, U., Bachu, S.: Geomechanical factors affecting geological storage of CO_2 in depleted oil and gas reservoirs. In: Canadian International Petroleum Conference, Petroleum Society of Canada (2004)

Hayes, R.E., Afacan, A., Boulanger, B., Shenoy, A.V.: Modelling the flow of power law fluids in a packed bed using a volume-averaged equation of motion. Transp. Porous Media **23**(2), 175–196 (1996). https://doi.org/10.1007/BF00178125

Hirasaki, G.J., Pope, G.A.: Analysis of factors influencing mobility and adsorption in the flow of polymer solution through porous media. Soc. Pet. Eng. J. **14**(4), 337–346 (1974)

Huang, H., Babadagli, T., Li, HA.: A quantitative and visual experimental study: effect of fracture roughness on proppant transport in a vertical fracture. In: SPE Eastern Regional Meeting, Society of Petroleum Engineers (2017)

Huang, X., Yuan, P., Zhang, H., Han, J., Mezzatesta, A., Bao, J.: Numerical study of wall roughness effect on proppant transport in complex fracture geometry. In: SPE Middle East Oil and Gas Show and Conference, Society of Petroleum Engineers (2017)

Huo, D., Gong, B.: Discrete modeling and simulation on potential leakage through fractures in CO_2 sequestration. In: Society of Petroleum Engineers, SPE Annual Technical Conference and Exhibition, 19–22 Sept, Florence, Italy, https://doi.org/10.2118/135507-MS (2010)

James, D.F., McLaren, D.R.: The laminar flow of dilute polymer solutions through porous media. J. Fluid Mech. **70**(4), 733–752 (1975). https://doi.org/10.1017/S0022112075002327

Karpyn, Z., Landry, C., Prodanović, M.: Induced rough fracture in Berea sandstone core. Retrieved from www.digitalrocksportal.org (2016)

Konzuk, J.S., Kueper, B.H.: Evaluation of cubic law based models describing single-phase flow through a rough-walled fracture. Water Resour. Res. **40**(2), W02402 (2004). https://doi.org/10.1029/2003WR002356

Kovscek, A.R., Tretheway, D.C., Persoff, P., Radke, C.J.: Foam flow through a transparent rough-walled rock fracture. J. Pet. Sci. Eng. **13**(2), 75–86 (1995). https://doi.org/10.1016/0920-4105(95)00005-3

Lavrov, A.: Non-Newtonian fluid flow in rough-walled fractures: a brief review. In: International Society for Rock Mechanics and Rock Engineering, ISRM SINOROCK 2013, 18–20 June, Shanghai, China (2013)

Lavrov, A.: Numerical modeling of steady-state flow of a non-Newtonian power-law fluid in a rough-walled fracture. Comput. Geotech. **50**, 101–109 (2013b). https://doi.org/10.1016/j.compgeo.2013.01.004

Lavrov, A.: Redirection and channelization of power-law fluid flow in a rough-walled fracture. Chem. Eng. Sci. **99**, 81–88 (2013c). https://doi.org/10.1016/j.ces.2013.05.045

Lavrov, A.: Radial flow of non-newtonian power-law fluid in a rough-walled fracture: effect of fluid rheology. Transp. Porous Media **105**(3), 559–570 (2014). https://doi.org/10.1007/s11242-014-0384-6

Lavrov, A.: Flow of truncated power-law fluid between parallel walls for hydraulic fracturing applications. J. Non-Newtonian Fluid Mech. **223**, 141–146 (2015). https://doi.org/10.1016/j.jnnfm.2015.06.005

Liu, Y., Sharma, M.M.: Effect of fracture width and fluid rheology on proppant settling and retardation: an experimental study. In: SPE Annual Technical Conference and Exhibition, Society of Petroleum Engineers (2005)

Liu, Y.: Settling and hydrodynamic retardation of proppants in hydraulic fractures. Ph.D. dissertation, University of Texas at Austin (2006)

Liu, S., Masliyah, J.H.: Non-linear flows in porous media. J. Non-Newtonian Fluid Mech. **86**(1), 229–252 (1999). https://doi.org/10.1016/S0377-0257(98)00210-9

Lopez, X., Valvatne, P.H., Blunt, M.J.: Predictive network modeling of single-phase non-Newtonian flow in porous media. J. Colloid Interface Sci. **264**(1), 256–265 (2003). https://doi.org/10.1016/S0021-9797(03)00310-2

Macosko, C.W.: Rheology: Principles, Measurements, and Applications. Wiley, London (1994)

Mirabolghasemi, M.: Micro-scale modeling of formation damage. Ph.D. dissertation, University of Texas at Austin (2017)

Noiriel, C., Gouze, P., Madé, B.: Time-resolved 3D characterisation of flow and dissolution patterns in a single rough-walled fracture. In: Krásný, J., Sharp, JM (eds) Groundwater in fractured rocks, IAH Selected Paper Series, vol 9 (Selected Papers on Hydrogeology), Taylor & Francis, London pp 629–642 (2007)

Noiriel, C., Gouze, P., Madé, B.: 3D analysis of geometry and flow changes in a limestone fracture during dissolution. J. Hydrol. **486**, 211–223 (2013). https://doi.org/10.1016/j.jhydrol.2013.01.035

Osiptsov, A.A.: Fluid mechanics of hydraulic fracturing: a review. J. Pet. Sci. Eng. **156**, 513–535 (2017). https://doi.org/10.1016/j.petrol.2017.05.019

Pearson, J.R.A., Tardy, P.M.J.: Models for flow of non-Newtonian and complex fluids through porous media. J. Non-Newtonian Fluid Mech. **102**(2), 447–473 (2002). https://doi.org/10.1016/S0377-0257(01)00191-4

Perrin, C.L., Tardy, P.M.J., Sorbie, K.S., Crawshaw, J.C.: Experimental and modeling study of Newtonian and non-Newtonian fluid flow in pore network micromodels. J. Colloid Interface Sci. **295**(2), 542–550 (2006). https://doi.org/10.1016/j.jcis.2005.09.012

Pipe, C.J., Majmudar, T.S., McKinley, G.H.: High shear rate viscometry. Rheol. Acta **47**(5–6), 621–642 (2008). https://doi.org/10.1007/s00397-008-0268-1

Raimbay, A., Babadagli, T., Kuru, E., Develi, K.: Quantitative and visual analysis of proppant transport in rough fractures. J. Nat. Gas Sci. Eng. **33**, 1291–1307 (2016). https://doi.org/10.1016/j.jngse.2016.06.040

Renshaw, C.E.: On the relationship between mechanical and hydraulic apertures in rough-walled fractures. J. Geophys. Res.: Solid Earth **100**(B12), 24629–24636 (1995). https://doi.org/10.1029/95JB02159

Rodríguez de Castro, A., Radilla, G.: Non-Darcian flow experiments of shear-thinning fluids through rough-walled rock fractures. Water Resour. Res. **52**(11), 9020–9035 (2016). https://doi.org/10.1002/2016WR019406

Rodríguez de Castro, A., Radilla, G.: Flow of yield stress and Carreau fluids through rough-walled rock fractures: prediction and experiments. Water Resour. Res. **53**(7), 6197–6217 (2017a). https://doi.org/10.1002/2017WR020520

Rodríguez de Castro, A., Radilla, G.: Non-Darcian flow of shear-thinning fluids through packed beads: experiments and predictions using Forchheimer's law and Ergun's equation. Adv. Water Resour. **100**, 35–47 (2017b). https://doi.org/10.1016/j.advwatres.2016.12.009

Roustaei, A., Chevalier, T., Talon, L., Frigaard, I.A.: Non-Darcy effects in fracture flows of a yield stress fluid. J. Fluid Mech. **805**, 222–261 (2016). https://doi.org/10.1017/jfm.2016.491

Seright, R.S.: Polymer gel dehydration during extrusion through fractures. SPE Prod. Facil. **14**(02), 110–116 (1999). https://doi.org/10.2118/56126-PA

Seright, R.S.: Gel propagation through fractures. SPE Prod. Facil. **16**(04), 225–231 (2001). https://doi.org/10.2118/74602-PA

Seright, R.S.: An alternative view of filter-cake formation in fractures inspired by Cr(III)-acetate-HPAM gel extrusion. SPE Prod. Facil. **18**(01), 65–72 (2003). https://doi.org/10.2118/81829-PA

Shukla, R., Ranjith, P., Haque, A., Choi, X.: A review of studies on CO_2 sequestration and caprock integrity. Fuel **89**(10), 2651–2664 (2010). https://doi.org/10.1016/j.fuel.2010.05.012

Sivanesapillai, R., Steeb, H., Hartmaier, A.: Transition of effective hydraulic properties from low to high Reynolds number flow in porous media. Geophys. Res. Lett. **41**(14), 4920–4928 (2014). https://doi.org/10.1002/2014GL060232

Sochi, T.: Non-Newtonian flow in porous media. Polymer **51**(22), 5007–5023 (2010). https://doi.org/10.1016/j.polymer.2010.07.047

Sochi, T.: Analytical solutions for the flow of Carreau and Cross fluids in circular pipes and thin slits. Rheol. Acta **54**(8), 745–756 (2015). https://doi.org/10.1007/s00397-015-0863-x

Sorbie, K.S., Clifford, P.J., Jones, E.R.W.: The rheology of pseudoplastic fluids in porous media using network modeling. J. Colloid Interface Sci. **130**(2), 508–534 (1989). https://doi.org/10.1016/0021-9797(89)90128-8

Talon, L., Auradou, H., Hansen, A.: Effective rheology of Bingham fluids in a rough channel. Front. Phys. 2(24). https://doi.org/10.3389/fphy.2014.00024 (2014)

Tokan-Lawal, A.O.: Understanding fluid flow in rough-walled fractures using X-ray microtomography images. Master thesis, University of Texas at Austin (2015)

Tokan-Lawal, A., Prodanović, M., Eichhubl, P.: Investigating flow properties of partially cemented fractures in Travis Peak Formation using image-based pore-scale modeling. J. Geophys. Res.: Solid Earth **120**(8), 5453–5466 (2015). https://doi.org/10.1002/2015JB012045

Tosco, T., Marchisio, D.L., Lince, F., Sethi, R.: Extension of the Darcy–Forchheimer law for shear-thinning fluids and validation via pore-scale flow simulations. Transp. Porous Media **96**(1), 1–20 (2013). https://doi.org/10.1007/s11242-012-0070-5

Wang, L., Cardenas, M.B., Slottke, D.T., Ketcham, R.A., Sharp, J.M.: Modification of the local cubic law of fracture flow for weak inertia, tortuosity, and roughness. Water Resour. Res. **51**(4), 2064–2080 (2015). https://doi.org/10.1002/2014WR015815

Wang, Y., Seright, R., Huang, B., Fu, C., Zeng, Y.: Describing flow behavior of polymer gel in fracture using rheology. J. Pet. Sci. Eng. **157**, 1209–1219 (2017). https://doi.org/10.1016/j.petrol.2017.08.019

Xiao, W., Xia, C., Wei, W., Bian, Y.: Combined effect of tortuosity and surface roughness on estimation of flow rate through a single rough joint. J. Geophys. Eng. **10**(4), 045015 (2013). https://doi.org/10.1088/1742-2132/10/4/045015

Yan, Y., Koplik, J.: Flow of power-law fluids in self-affine fracture channels. Phys. Rev. E **77**(3), 036–315 (2008). https://doi.org/10.1103/PhysRevE.77.036315

Zhao, J., Kang, Q., Yao, J., Viswanathan, H., Pawar, R., Zhang, L., Sun, H.: The effect of wettability heterogeneity on relative permeability of two-phase flow in porous media: a lattice Boltzmann study. Water Resour. Res. **54**(2), 1295–1311 (2018)

Zhou, J.Q., Hu, S.H., Fang, S., Chen, Y.F., Zhou, C.B.: Nonlinear flow behavior at low Reynolds numbers through rough-walled fractures subjected to normal compressive loading. Int. J. Rock Mech. Min. Sci. **80**, 202–218 (2015). https://doi.org/10.1016/j.ijrmms.2015.09.027

Zimmerman, R.W., Bodvarsson, G.S.: Hydraulic conductivity of rock fractures. Transp. Porous Media **23**(1), 1–30 (1996). https://doi.org/10.1007/BF00145263

Zimmerman, R.W., Kumar, S., Bodvarsson, G.S.: Lubrication theory analysis of the permeability of rough-walled fractures. Int. J. Rock Mech. Min. Sci. Geomech. Abstr. **28**(4), 325–331 (1991). https://doi.org/10.1016/0148-9062(91)90597-F

Zou, L., Jing, L., Cvetkovic, V.: Roughness decomposition and nonlinear fluid flow in a single rock fracture. Int. J. Rock Mech. Min. Sci. **75**, 102–118 (2015). https://doi.org/10.1016/j.ijrmms.2015.01.016

Affiliations

Min Zhang[1] (iD) **· Maša Prodanović[1] · Maryam Mirabolghasemi[2] · Jianlin Zhao[3]**

Maša Prodanović
masha@utexas.edu

Maryam Mirabolghasemi
maryam@che.msstate.edu

Jianlin Zhao
zjlsetoff@163.com

[1] Hildebrand Department of Petroleum and Geosystems Engineering, The University of Texas at Austin, Austin 78712, USA

2 Dave C. Swalm School of Chemical Engineering, Mississippi State University, Starkville 39762, USA

3 Chair of Building Physics, Department of Mechanical and Process Engineering, ETH Zurich (Swiss Federal Institute of Technology in Zurich), 8093 Zurich, Switzerland